Reversible rock-slope deformations caused by cyclic water-table fluctuations in mountain slopes of the Central Alps, Switzerland

Juergen Hansmann · Simon Loew · Keith F. Evans

Abstract Within the framework of the Gotthard Base Tunnel Project in the Central Alps, Switzerland, geodetic monitoring networks were installed above the tunnel trajectory in alpine valleys. Natural ground-surface deformation recorded in the years prior to the tunneling excavation was seen to contain an unexpectedly large cyclical component of horizontal strain across the valleys, which was seasonal and appeared to be due to elastic processes. The strain is strongly correlated with snow melt and rainstorm precipitation, suggesting the implied rock-mass deformation is driven by changes in water-table elevation within adjacent mountain slopes. The horizontal strains are of the order of $1–2{\cdot}10^{-5}$, which is close to the design limits that can be accommodated by hydropower arch dams in the study area. This study investigates these processes in detail and describes a new mathematical model (REROD), which is able to accurately reproduce and predict such natural rock-slope displacements. The model implements a transfer-function approach to predict the valley-crossing strains from rainfall and winter snow height data recorded at nearby meteorological stations. It has been used to estimate and remove the natural strain signal from the net recorded deformation so as to resolve the component due to tunneling.

Keywords Groundwater recharge · Fractured rock · Hydro-mechanical coupling · Geodetic measurement · Switzerland

Introduction

High precision leveling surveys above the Gotthard highway tunnel, Switzerland, which was built between 1970 and 1977 in crystalline rocks, revealed the occurrence of up to 12 cm of subsidence above the 200–600-m-deep tunnel (Zangerl et al. 2003, 2008a, b). The subsidence appears to be a consequence of the drainage of the crystalline rock mass around the tunnel, the large reduction in fluid pressure giving rise to volumetric deformation and the mobilizing of shear movement on faults (Zangerl et al. 2003, 2008a, b). Such large ground deformations can cause severe damage to large-scale sensitive structures, particularly concrete arch dams (Lombardi 1992a, b, 2004) even though the tunnel may be driven several kilometers away from the structure.

A new, deeper tunnel, the Gotthard Base Tunnel, was recently excavated in the Central Alps. Since the tunnel trajectory passes close to three large arch dams and hydropower storage lakes at depths of 1.0–1.5 km, surface deformations at these locations are carefully monitored to detect any deformation that might be caused by tunneling operations (Braeker 2006; Studer and Braeker 2007). For this purpose, six high-precision geodetic networks have been set up in three valleys (Val Curnera, Val Nalps, and Val Termine/Santa Maria) as shown in Fig. 1. The Gotthard Base Tunnel consisting of two parallel tubes with a lateral distance of approximately 50 m is represented by one single dashed black line in Fig. 1 for clarity.

All networks are located in the crystalline basement of the Gotthard Massif. Each local network consists of 1 or 2 total stations (i.e. automated tachymeter stations that monitor all reflectors in their network) and up to 10 reflectors placed at different elevations above the valley floor and at various distances from the dam sites (Braeker 2006; Studer and Braeker 2007). The cross-valley distances of reflectors on opposing valley slopes range from 100 to 1,000 m. In every valley, reflectors are located close to the valley bottom, at 30–50 m elevation above the valley floor, and in higher parts (150–250 m) of the valley flanks (Fig. 2). The total stations automatically measure the relative position of all reflectors in their network every night, when meteorological conditions are most stable. Consequently relative movements of the reflectors within each network are tracked with a diurnal resolution for the profiles in Val Termine and Santa Maria, although data are only available with a 2-week sampling period for Val Nalps and Val Curnera.

The networks became operational several years before tunneling-related deformation was expected in order to

Received: 4 April 2011 / Accepted: 19 October 2011
Published online: 8 November 2011

J. Hansmann (✉) · S. Loew · K. F. Evans
Engineering Geology, Department of Earth Sciences,
Swiss Federal Institute of Technology, ETH Zürich,
Sonneggstrasse 5, 8092 Zürich, Switzerland
e-mail: Juergen.Hansmann@erdw.ethz.ch
Tel.: +41-44-6333865

 DOI 10.1007/s10040-011-0801-7

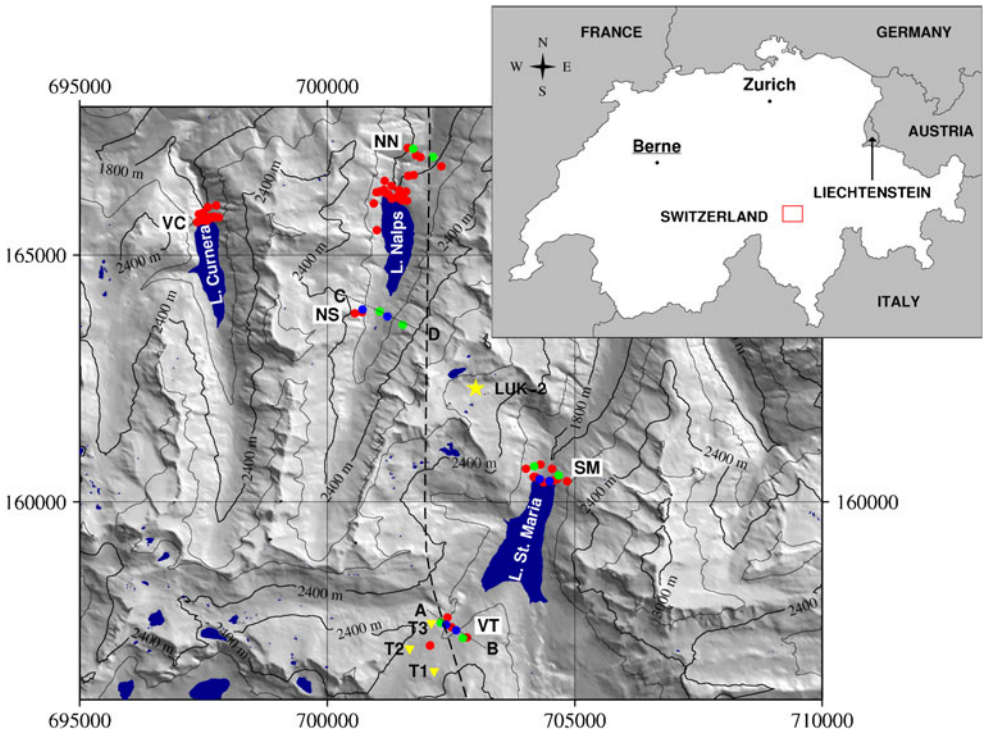

Fig. 1 Map of the study area. *Blue and green dots* are the reflectors of the geodetic monitoring system that are the subject of this study. *Red dots* indicate the position of other reflectors. Local monitoring networks are: Nalps North (*NN*), Nalps South (*NS*), Santa Maria (*SM*), Val Termine (*VT*), Val Curnera (*VC*). The *yellow star* marks the position of the Swiss Snow and Avalanche Research Institute (SLF) snow height measuring station LUK-2 at 2,550 m a.s.l., while the *black dashed line* is the trace of the two-tube Gotthard Base Tunnel. The three *yellow triangles* in VT mark the position of ground temperature loggers. Along the profiles from *A* to *B* and *C* to *D*, snow height measurements were conducted (as shown in Fig. 7). The dam walls are located at the northern sides of the lakes. Blue areas represent lakes. *Inset top right*: map of Switzerland with a *red box* indicating the study area

characterize the noise level and natural deformations. During this period, unexpectedly large natural ground-surface deformations between reflector pairs of these cross sections were observed at predominantly annual periods. The implied deformation was found to be largely reversible, systematic and not related to local slope instabilities. However, a strong correlation with the timing and amount of spring snow melt and summer rainstorm precipitation was observed (Loew et al. 2007). This is evident in Fig. 3 which shows the horizontal displacement measured across Val Termine (black lines), the weekly rainfall (gray bars in Fig. 3a) and the snow height at the nearby gauging station (gray, filled curve in Fig. 3b). Rainfall is measured at the Santa Maria dam site and the snow height is recorded at the Swiss Snow and Avalanche Research Institute (SLF) station LUK-2, shown in Fig. 1. Loew et al. (2007) and El Tani and Bremen (2006) proposed that the deformations were driven by changes in the water table in the fractured aquifers in the mountain slopes adjacent to the valleys caused by seasonally varying recharge and aquifer depletion conditions. A detailed conceptual model of this deformation is discussed later.

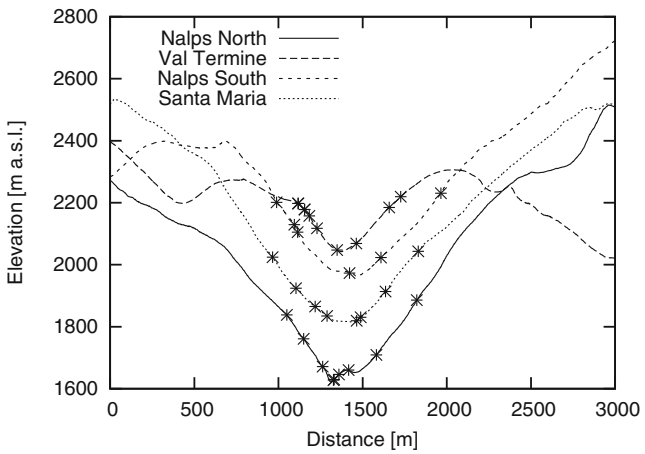

Fig. 2 Topographic profiles across Val Termine (VT), Santa Maria (SM), Nalps North (NN) and Nalps South (NS) at the locations of the geodetic networks. The positions of reflectors along the profiles are indicated by *star symbols*

During the period when tunneling advanced beneath the monitoring locality, any tunnel-related deformation would be superposed on the natural fluctuations. Thus, detection of the development of a deformation component related to the advance of the tunnel would be hindered to some degree by the natural fluctuation signals. To help improve the resolvability of a tunnel-related component in the measured signal, a predictive model was developed that allowed the component due to natural deformations to be estimated from measurable meteorological data. Since the most significant component of the natural deformation is horizontal and normal to the valley axis, the direction that is of greatest concern for concrete arch dam safety, the

 DOI 10.1007/s10040-011-0801-7

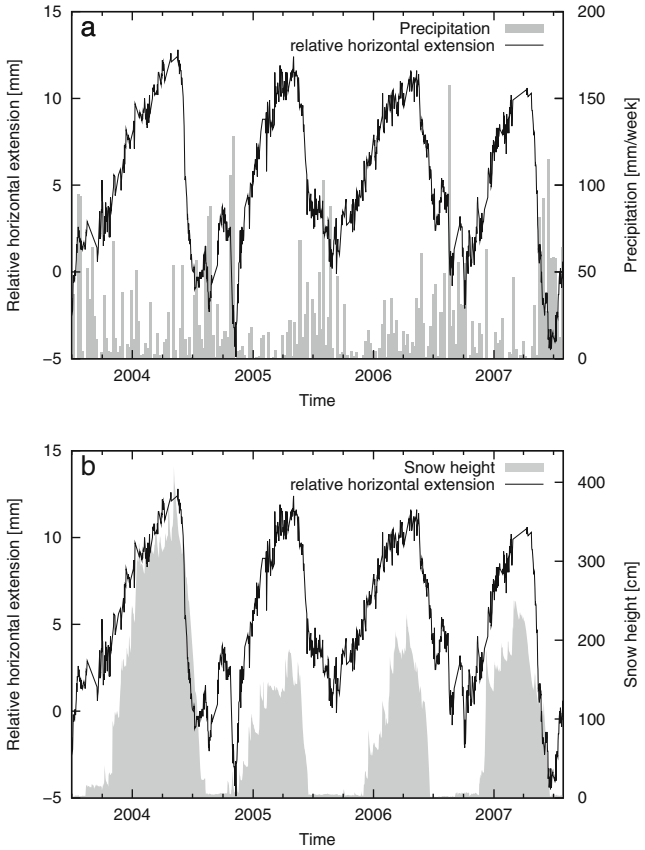

Fig. 3 Relative horizontal displacement normal to the valley axis measured between mid 2003 and mid 2007 in Val Termine together with **a** 7-day averaged precipitation measured at Santa Maria dam and **b** snow height measurements at SLF station LUK-2 (at 2,550 m a.s.l)

model focused on predicting this component. The model is mathematical rather than physical in formulation, and predicts the expected natural horizontal relative displacement across each valley profile based upon local rainfall and snow height data. The deformations are considered to result from three key processes: (1) infiltration of snow melt water, (2) infiltration from summer rainstorms during snow-free periods, and (3) depletion of the groundwater reservoir during times when there is no recharge. This model is described later and shows that it yields good predictions for the natural deformations, even outside the time window used to calibrate the model parameters.

Hydrology of the study area

Geological and hydrogeological conditions

The main focus of this paper is the data obtained in the Val Termine valley in the canton Ticino of the Central Alps, and supporting information from the Santa Maria and Val Nalps cross sections, located in canton of Grison. As shown in Fig. 1, all valleys are located close to the tunnel trajectory and in the tectonic unit of the Gotthard Massif. Due to the high elevation (1,600–2,600 m a.s.l.) and steep topography with large debris fans, there is little vegetation in the monitoring locations. Detailed field work has been conducted in Val Termine with the focus on determining the fracture patterns and the elevation of the groundwater level after long time spans without rainfall as well as immediately after strong rainstorm events. In the Val Termine section, the surface outcrops mainly consist of Caledonian gneisses (granitic striped gneisses) with a distinctive lineation of minerals and a high degree of jointing. Quaternary moraines partly cover the south eastern part of the valley. Four joint sets have been identified with a mean spacing ranging between 1.6 and 5.8 m and a mean observable persistence of 2.6–6.8 m (Table 1). The angle θ in Table 1 is the angle between the strike of the fracture set and the axis of the valley in question. Table 1 also lists the joint sets in Val Nalps that were identified by Schneider (1993). Mean spacing and persistence have not yet been measured at this location. According to Schneider (1993), the steep joint sets dominate in the Val Nalps cross sections.

Figure 4 shows the mapped position of springs and groundwater seeps, and the inferred spring lines in Val Termine. The topographic elevation of the spring lines indicates the position of the groundwater level at the intersection with the ground surface. As Fig. 4 illustrates, the groundwater level can drop down to the valley bottom in dry periods, but may move to an elevation 150–200 m above the valley bottom within several days after strong summer rainstorms. It is likely that even higher spring-line elevations are realized during and shortly after snow melt, but mapping the spring lines is not possible when the melting snow still covers major parts of the slopes.

Climatic conditions

Precipitation measurements are automatically recorded by stations at the hydropower storage lake dams. Figure 5 shows the precipitation record for the Santa. Maria and Nalps dam sites. Rainstorm events with 100–200 mm of precipitation per week (sometimes even more) are common in both valleys during the summer snow-free season. Some local variations can be observed in the two valleys, but in most cases, timing and precipitation volume of heavy rainstorm events are quite similar.

The snow height data used in this study comes from the station LUK-2 (Fig. 1). Field measurements in Val Termine show that the snow height and the evolution of the snow cover varies a lot on the catchment scale and along the cross sections. This is illustrated with measurements from three ground (subsurface) temperature loggers (T1, T2 and T3) that were installed in Val Termine (Fig. 1) in winter 2008/2009. One temperature logger (T1) was located on a north-west facing slope, one logger (T2) on a south-east facing slope, and the third temperature logger (T3) on a north-east facing slope. Their elevations range from 2,270 to 2,305 m a.s.l. The daily averaged temperature signal recorded by these three loggers is plotted against the measured snow height at the SLF station LUK-2 in Fig. 6. The loggers register a constant temperature signal of around 0°C when covered with snow but show daily averaged temperatures significantly above 0°C once

 DOI 10.1007/s10040-011-0801-7

Table 1 Observed joint sets in Val Nalps (Schneider 1993) and Val Termine

Valley	Joint set name	Main orientation (dip direction/dip angle)	Mean spacing [m]	Mean persistence [m]	θ [°]
Val Nalps	KIa	250/75			53
	KIb	270/70			17
	KII	75/80			32
	KIII	130/60			23
Val Termine	KIb	255/60	1.8	2.8	35
	KII	70/65	1.7	2.6	60
	KIII	125/85	1.6	2.9	5
	KIV	185/55	5.8	6.8	55

exposed by the snow melt. It is evident in Fig. 6 that the end of snow melt varies by at least 2 months, even on a local scale. The spatial variability of snow height was also shown by conducting measurements of snow height along valley-crossing profiles close to the bottom of Val Termine and Val Nalps South. The measurements were made with an avalanche probe on 28 and 29 April 2010. The results are shown in Fig. 7. In Val Termine no significant difference in mean snow height between the two slopes existed at the time of mapping, whereas in Val Nalps the north-west exposed slope obviously accumulated more snow than the south-east exposed slope. It is likely that the snow cover on both mapped slope sections also includes snow avalanche deposits.

Observed displacements and strains

Local tachymetric networks

The entire monitoring network includes automatic tachymeters, borehole extensometers, high-precision leveling, and differential global positioning systems (Braeker 2006; Studer and Braeker 2007). Of relevance here are the results of the total station measurements of six local tachymetric networks installed in 2000 and 2001. These local networks are either located at the dam sites or 1–3.5 km in front of (north or south of) the dams and serve to monitor deformations within cross sections perpendicular to the valley axes (Fig. 1).

The total station measurements are designed to monitor local deformations at a resolution that allows assessment of dam safety in the project area. Static analyses showed that the limits of elastic compression along the crest of the three dams ranges from 35 to 70 mm, and the limits of elastic extension from 10 to 20 mm. For this reason, the geodetic monitoring system was designed for a significance level of 4 mm, i.e. for each local network, the system should be able to detect changes in relative position and height between any pair of points for any measurement period whenever they exceed 4 mm. In fact, the resolution of changes in relative position between pairs of points is better than this. The total station used in the measurements is a Leica TCA2003 which has an angular accuracy of 2.3 μrad and a distance measurement accuracy of 1.6 mm over the 600 m length of the longest line of relevance to this study. The measurements are conducted at night when environmental conditions are most stable. As the tunnel-induced deformations can become effective within days or weeks, the monitoring system has been designed to deliver data on a daily basis,

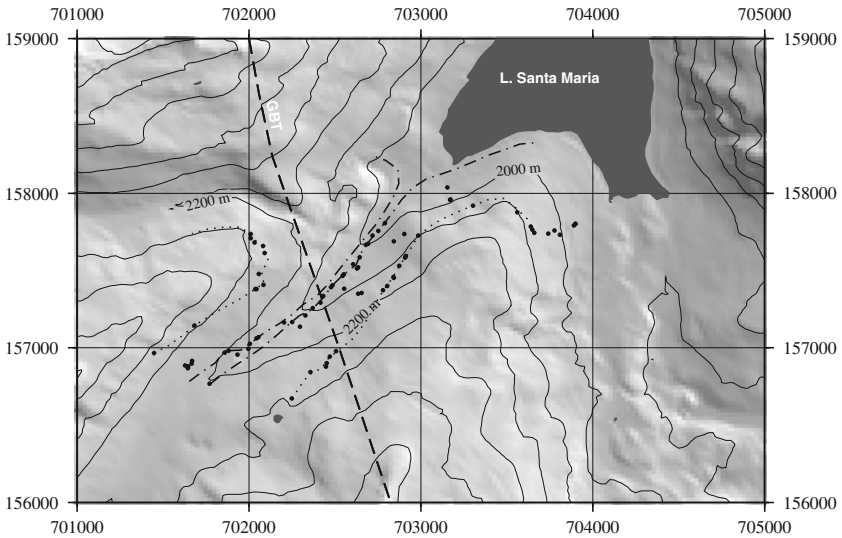

Fig. 4 Mapped springs and groundwater seepage locations in Val Termine. The *dotted lines* show the interpolated positions of the spring line after some days of strong rainfall (September 2008). The *thick dashed-dotted lines* at the valley bottom show the position after a long, dry period (October 2009). The *single black dots* are the locations at which the springs were measured. The *thick black dashed line* crossing from north to south represents the Gotthard Base Tunnel (GBT) trajectory

 DOI 10.1007/s10040-011-0801-7

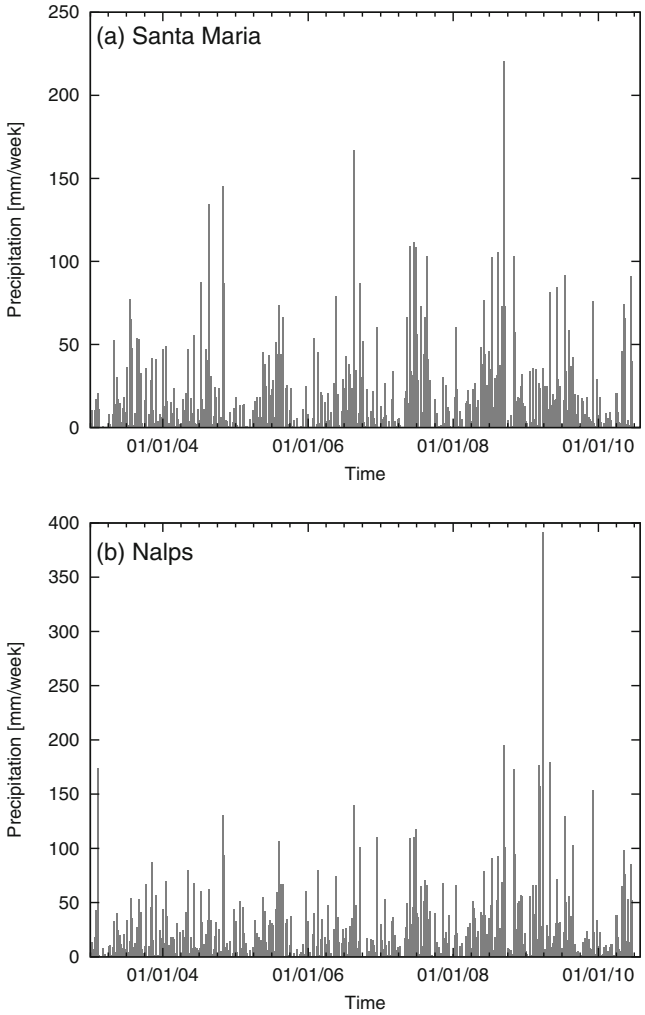

Fig. 5 Weekly precipitation recorded at the hydropower storage lake dams of **a** Santa Maria and **b** Nalps

even during winter time. However, the data for Nalps-North and Nalps-South are processed with a fortnightly sampling period.

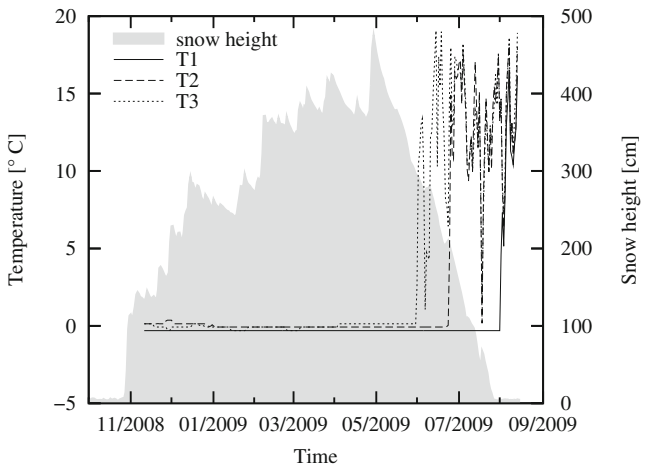

Fig. 6 Record of mean daily temperature recorded by the temperature loggers T1, T2 and T3 (see Fig. 1) at Val Termine, together with snow height from SLF station LUK-2 during winter 2008/2009

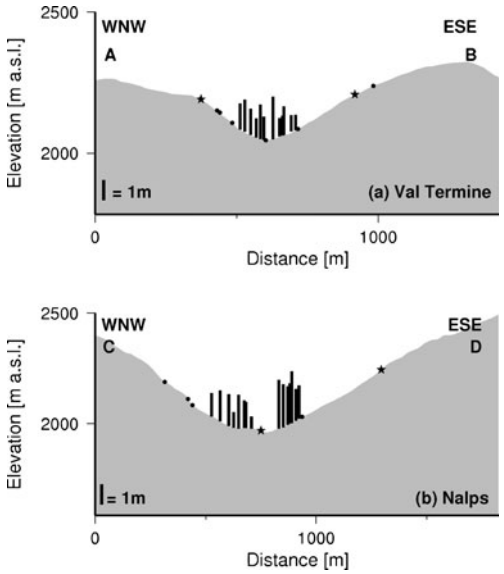

Fig. 7 Snow height (*black bars*) measured along profiles A–B and C–D (located in Fig. 1) on 28 and 29 April 2010, respectively. The *black dots* denote the position of reflectors projected into the profile lines. The *stars* are the reflector pairs whose relative horizontal displacement was fitted by the mathematical model

The local relative deformations between all points of a network are measured with one automatic total station at the valley bottom (Nalps South, Nalps North) or valley flank (Val Termine). The high-precision tachymeter measurements are carried out from 8 pm to 8 am in hourly periods. Data processing is based on the program LTOP of Swisstopo (Gubler 2003) and includes atmospheric corrections (air temperature, pressure, humidity). Details of the monitoring system and data processing are described in AlpTransit (2003).

Deformation signal

Figure 8 illustrates a baseline of length L across the valley between two reflectors. Changes in the relative locations of the reflectors, which define the relative displacement vector, can be decomposed into its three components with respect to a local coordinate system (x, y and z) where x is horizontal and oriented across the valley, y is horizontal and parallel to the valley strike, and z which is up. These three components are referred to as ΔL_x, ΔL_y and ΔL_z respectively. The components of the relative displacement that were recorded in the sections Val Termine, Santa Maria Dam, Nalps North and Nalps South are shown in Fig. 9.

All measurements show periodic, reversible deformations at annual periods. At all sites except possibly Santa Maria, the most significant relative displacement component is horizontal and normal to the valley axis. This component shows a maximum compression (i.e. movements of valley slopes towards each other) in early summer and maximum extension (i.e. slopes move away from each other) in late winter time. At Nalps North and Nalps South, an irreversible trend in the horizontal components of deformation is visible from the second

DOI 10.1007/s10040-011-0801-7

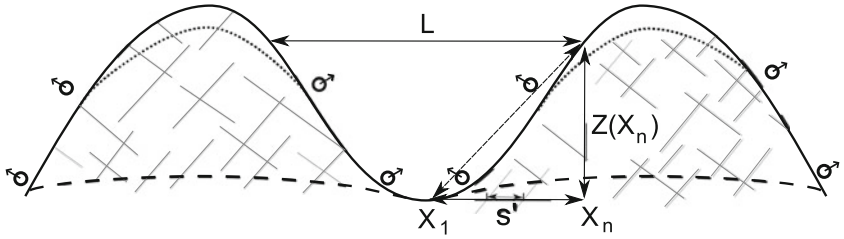

Fig. 8 Illustration of problem geometry showing maximum (*dotted line*) and minimum (*dashed line*) water-table surfaces within the rock mass, and the corresponding locations of springs (*circles with arrows*). The horizontal line of length L represents the distance between a reflector pair. Changes in the relative location of the end points define the relative displacement vector which has components ΔL_x (horizontal, cross-valley), ΔL_y (horizontal, along-valley) and ΔL_z (vertical). The *triangle* approximates the shape of the slope, and is used for the calculations in section Deformation from mapped joint sets

half of the year 2005 in Nalps North, and from the end of the year 2008 in Nalps South, which can be explained by the nearby tunnel excavation and associated rock mass drainage (see section Discussion and conclusions).

The horizontal, cross-valley relative displacement amplitudes are largest in Val Termine, where values of 10–16 mm are seen. Figure 9 also shows that the amplitude of the cross-valley displacements is larger for reflector pairs at higher elevations and larger distances L compared to pairs closer to the valley floor, which span shorter distances. The implied horizontal strains (i.e. the valley-crossing horizontal and vertical relative–displacement components divided by the distance between monitoring points) are similar for all reflector pairs at a given site, but differ between sites. The horizontal strains are largest in Val Termine and have a similar magnitude (up to $2 \cdot 10^{-5}$).

Rainfall response time

In order to quantify the response time of the deformation signals to summer rainstorms, several cross-correlation analyses were conducted on diurnally sampled datasets from Val Termine and Santa Maria. The data from the other valleys could not be used owing to the fortnightly sampling period. The results of these calculations are shown in Fig. 10.

The cross correlation coefficient $R_{xy}(\tau)$ is defined as:

$$R_{xy}(\tau) = \lim_{w\to\infty} \int_{-w/2}^{w/2} x(t) \cdot y(t+\tau)dt \qquad (1)$$

where x is the deformation signal and y the rainfall signal, w is a time window, and τ is a time lag. For a discrete series of n points, R_{xy} (τ) can be calculated from:

$$R_{xy}(\tau) = \frac{\sum_{t=1}^{n} x(t) \cdot y(t+\tau)}{\sqrt{\sum_{t=1}^{n} x(t)^2 \cdot \sum_{t=1}^{n} y(t+\tau)^2}} \qquad (2)$$

Several large rainstorm events with volumes from 17 to 134.2 mm that occurred during snow-free periods were sampled from the daily precipitation records at Val Termine and Santa Maria. The correlations were performed for time windows containing single rainstorms. The deformation signal was taken as ΔL_x, the horizontal, valley-crossing component of relative displacement. Figure 10 shows that, in both valleys, the rainfall signal correlates best with the deformation signal when the time lag is 0 days, i.e. the deformation signal responds to a summer rainstorm within the first 24 h. The correlation between the rainfall and deformation series in 2005 was somewhat different for the two valleys. The reason for this might be local variations in the precipitation patterns.

The response times of the deformation signal to snow melt derived from cross-correlation are not so well-defined as for rainfall, most likely because the relationship of snow height to recharge is complex and depends upon other factors, particularly altitude, exposition to solar radiation and permeability of the frozen ground surface at the base of the snow pack. Compaction and wind transport can also contribute to reduced snow height at the measuring station without generating recharge.

Conceptual model

A sketch of the water-table elevation within the valley flanks at different times of the year is shown in Fig. 8. The dashed line marks the water table at a low position, close to the valley bottom, during dry periods without recharge e.g. during late summer or in winter when a snow cover has been established and no infiltration occurs. The dotted line denotes the water table after recharge, due to either snow melt in late spring or summer rainstorms.

As the response time of the deformation signal to rainstorm or snow melt recharge is very short, it is assumed that the infiltration through the unsaturated zone is fast, and that the deformation is generated in the higher permeability (upper) parts of the fractured rock mass. As shown in Masset and Loew (2010), the depth of this zone, which is characterized by higher fracture frequencies and apertures, can reach up to 400 m below ground surface. When the water table rises and the fluid pressure inside the rock mass is increased by recharge, the effective normal stress acting on the fractures decreases and the apertures increase. Consequently, the rock mass expands and the distance between reflectors on opposing sides of the valley

 DOI 10.1007/s10040-011-0801-7

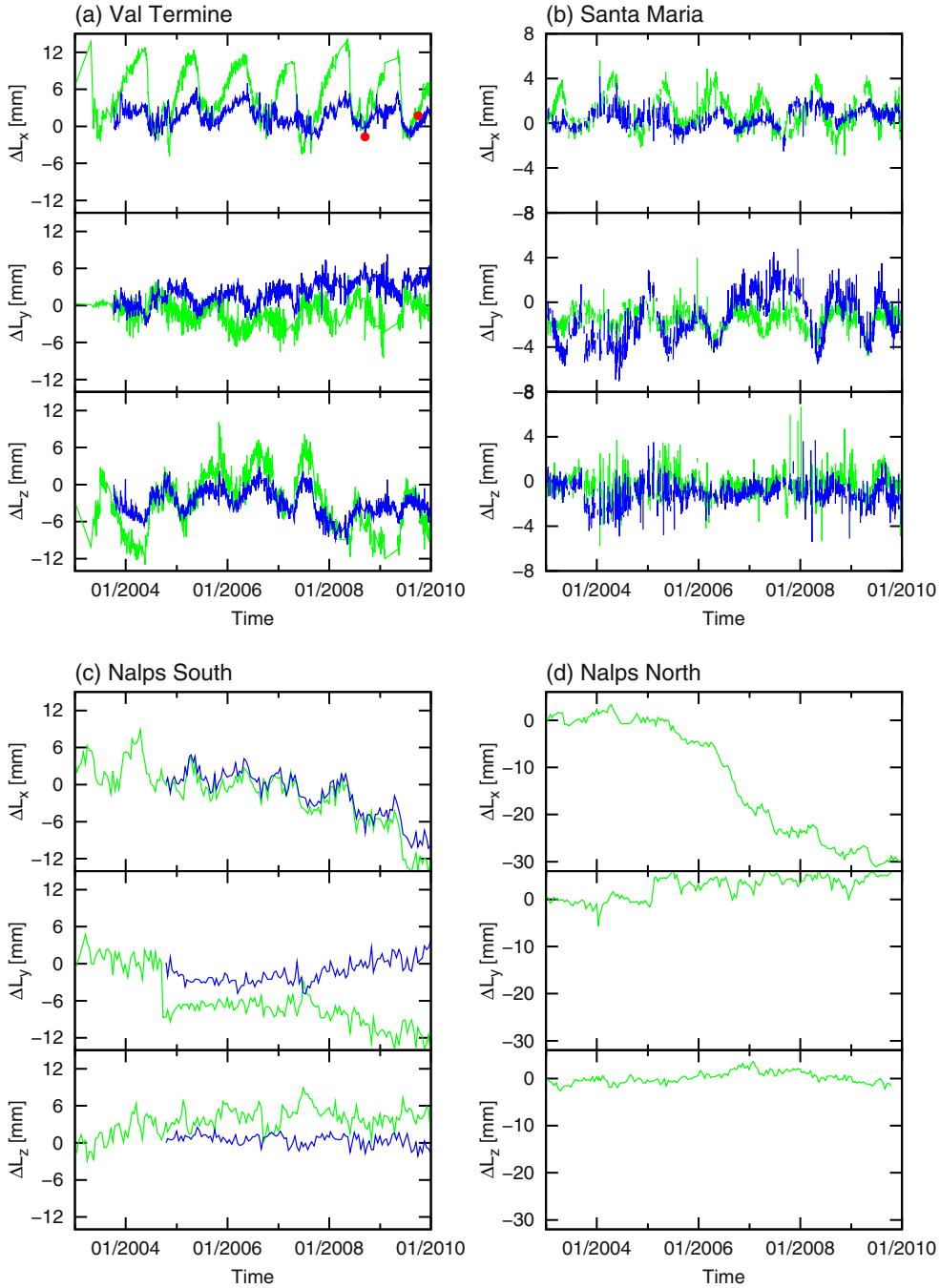

Fig. 9 Three components of the relative displacement of reflector pairs measured in **a** Val Termine, **b** Santa Maria, **c** Nalps South and **d** Nalps North, between 2003 and 2010. The *green line* shows data from reflector pairs marked in green in Fig. 1; the *blue line* shows data from reflector pairs closer to the valley bottom, marked in blue in Fig. 1. The reflector elevations and line lengths are indicated. The *red points* at Val Termine mark the times when the spring line measurements (Fig. 4) were performed

decreases. When the fluid pressure decreases during depletion of the groundwater reservoir, the effective normal stress on the fractures increases and they tend to close, thereby increasing the distance between opposing reflector pairs.

To evaluate the factors that control the process, a simple quantitative model was developed to determine whether the observed length changes of valley-crossing baselines can be explained as the net effect of aperture changes of the mapped fracture distribution for reasonable fracture stiffness characteristics.

Stress dependent opening and closure of fractures

Figure 11 shows the effective normal stress that acts on a fracture that dips at an angle β within a medium in which the local horizontal stress is σ_h and the vertical stress is σ_v.

 DOI 10.1007/s10040-011-0801-7

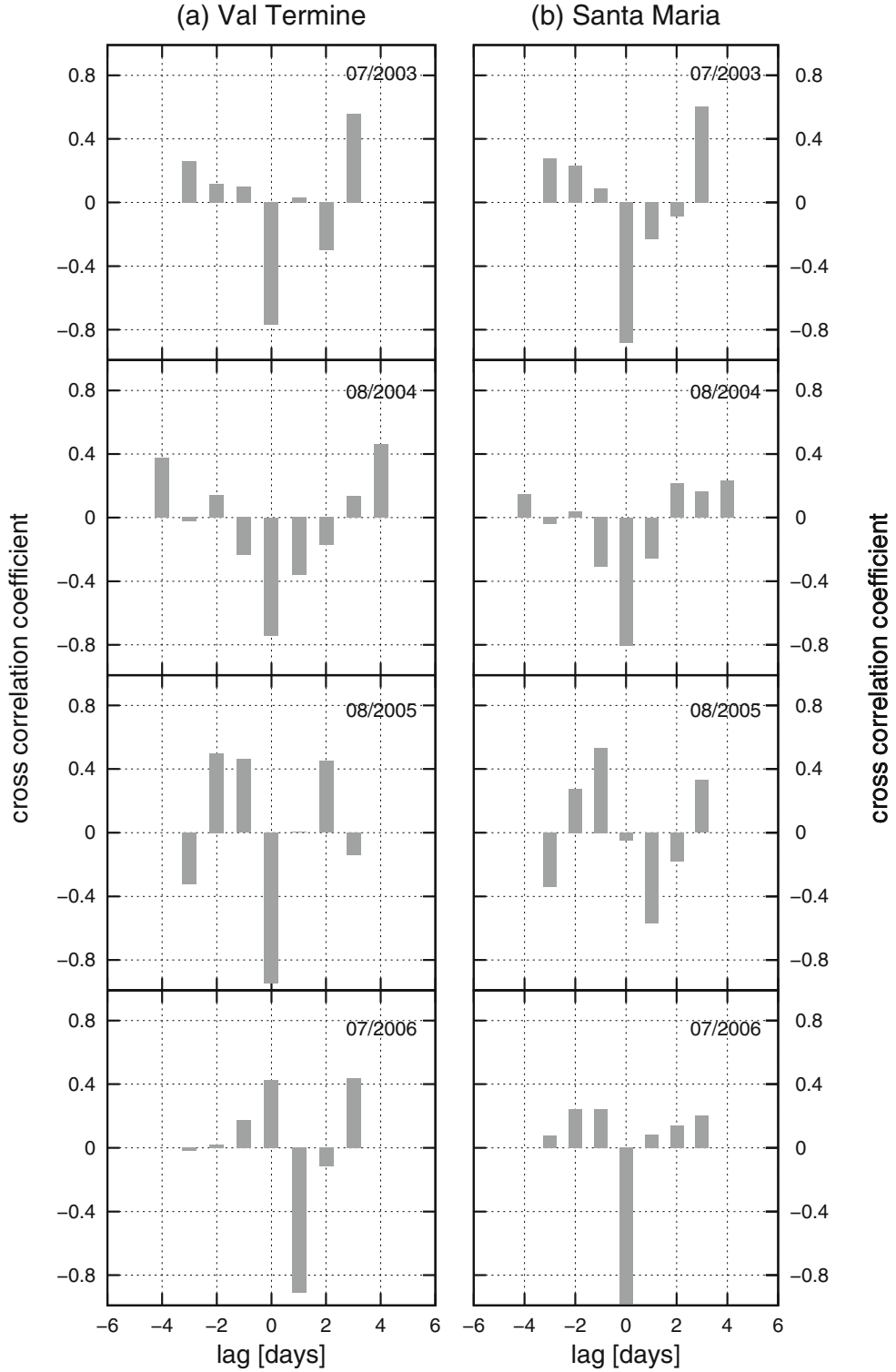

Fig. 10 Results of cross correlation analysis of deformation signal and rainfall data in **a** Val Termine and **b** Santa Maria

The normal stress on the fracture shown in Fig. 11 is:

$$\sigma_n = \frac{\sigma_V+\sigma_h}{2} + \frac{\sigma_V-\sigma_h}{2}\cos(2\beta) \quad (3)$$

The effective normal stress, σ_n' that acts on a fracture at a depth z in a rock of density ρ_r where the fluid pressure p_p is given by $\sigma_n'=\sigma_n - p_p$, and can be written in terms of the total stress ratio, $k_0=\sigma_h/\sigma_V$, as,

$$\sigma_n^{'} = \left[\left(\frac{1+k_0}{2} + \frac{1-k_0}{2}\cos(2\beta)\right)\cdot \rho_r g z\right] - p_p \quad (4)$$

where g is the acceleration due to gravity constant. The change of the effective normal stress from an initial value

 DOI 10.1007/s10040-011-0801-7

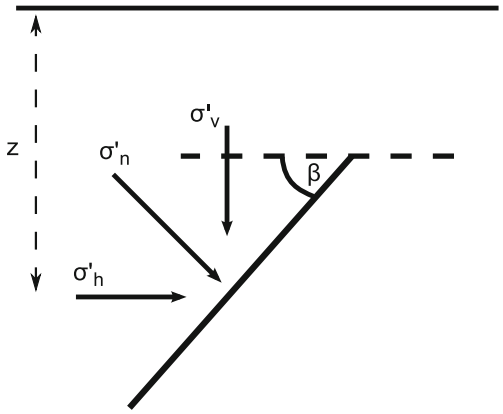

Fig. 11 Effective normal (σ'_n), vertical (σ'_v) and horizontal (σ'_h) stresses on a fracture plane with an inclination angle β and depth z. As the fluid pressure inside the rock mass changes due to depletion or recharge, the effective stresses and therefore the fracture aperture change as well

σ_{ni} to a new value σ_n' causes a change in mechanical aperture Δa_m of the fracture, which can be calculated from the semi-logarithmic closure law (Zangerl et al. 2008c):

$$-\Delta a_m = \frac{1}{dk_n/d\sigma_n'} \ln\left(\frac{\sigma_n'}{\sigma_{ni}'}\right) \quad (5)$$

where k_n is fracture normal stiffness and $dk_n/d\sigma_n'$ is a constant referred to as the 'stiffness characteristic' (Zangerl et al. 2008c; Evans et al. 1992).

The model geometry is shown in Fig. 8. The rock masses that constitute the valley flanks are approximated as triangular in form and rise with a constant slope from the centre of the valley to the peaks that flank the valley. The latter attain a height z_{max} above the valley floor at a horizontal distance x_{max} from the valley centre. At Val Termine, the peaks have an elevation of ~2,300 m a.s.l. and the valley floor is at 2,050 m a.s.l. giving z_{max}=250 m.

An approximation to the valley-normal deformation can be obtained by summing the pressure-induced changes in aperture of all fractures that lie at the level of the valley floor within a distance of x_{max} from the valley centre (i.e. all fractures that intersect the base of the triangles). The effects of shear and fracture interactions are excluded. The maximum variation in groundwater level that can occur during the annual cycle is given by assuming that the groundwater level is at the level of the surface when the aquifer is fully recharged, and declines to the level of the valley after prolonged periods without recharge. Thus, at the level of the valley, the maximum variation in pore pressure within the rock mass increases with distance x_{max} from the valley centre, and is given by

$$\Delta p_p(x) = \rho_f g\left(\frac{z_{max}}{x_{max}}\right)x \quad (6)$$

If poro-elastic effects are neglected so that pore pressure changes do not affect the total stress, then the corresponding variation in effective normal stress acting on a fracture at a distance 'x' along the profile from the valley centre would be,

$$\Delta\sigma_n'(x) = \rho_f g\left(\frac{z_{max}}{x_{max}}\right)x \quad (7)$$

With a fluid density ρ_f of 1,000 kg m^{-3}, the change in effective normal stress caused by the maximum possible change in water-table elevation below the peaks (i.e. x=x_{max}) in Val Termine would be 2.45 MPa.

The aperture change of a fracture resulting from the maximum change in effective normal stress is given by Eq. 5 and depends upon the stiffness characteristic of the fracture and the absolute normal stress level supported by the fracture. The latter depends upon the fracture orientation, and also on the distance, x, of the fracture from the valley centre owing to increasing overburden. The initial effective normal stress, σ'_{ni}, is taken as the case when the water table within the valley flanks is at the level of the valley floor. For a fracture of dip β that lies at the elevation of the valley floor, the initial normal effective stress is obtained from Eq. 4 by setting p_p=0:

$$\sigma_{ni}'(x) = \left(\frac{1+k_0}{2} + \frac{1-k_0}{2}\cos(2\beta)\right)\cdot\rho_r g x(z_{max}/x_{max}) \quad (8)$$

Deformation from mapped joint sets

The contribution to valley-normal displacement from each fracture that intersects the base profile depends upon its orientation. Consider a fracture plane that dips at an angle β in a direction that subtends an angle θ with the azimuth normal to the valley axis (i.e. the angle between the fracture strike and the valley axis). Then pressure-induced aperture change, Δa_m, which can be viewed as a dislocation vector oriented normal to the fracture plane, can be resolved into the x, y and z components (i.e. valley-crossing horizontal, valley-parallel horizontal, and vertical respectively) using the following relations:

$$\begin{aligned}\Delta a_{mx} &= \cos(\theta)\cdot\cos(90-\beta)\cdot\Delta a\\ \Delta a_{my} &= \sin(\theta)\cdot\cos(90-\beta)\cdot\Delta a\\ \Delta a_{mz} &= \sin(90-\beta)\cdot\Delta a\end{aligned} \quad (9)$$

For each of the fracture sets listed in Table 1, the average distance between fractures measured along the base of the triangle, s′, will be related to the fracture spacing, s, by:

$$s' = s/\sin(\beta)\cos(\theta) \quad (10)$$

The change in distance between two points,ΔL_x, separated by a distance L on opposite sides of the valley due to fluid pressure changes in the flanks, is assumed to be given by summing the resulting aperture changes of all fractures that intersect the base of the triangle between

 DOI 10.1007/s10040-011-0801-7

$x=-L/2$ and $x=L/2$. If a given set has a spacing along the base of s′, then there will be $L/2$ s′ fractures contributing in each flank. The net change in line length from both flanks is thus:

$$\Delta L_{\mathrm{x}} = 2\left(\sum_{\mathrm{n}=1}^{\mathrm{L}/2s'} \Delta a_{\mathrm{x}}(x = ns')\right) \tag{11}$$

where

$$\Delta a_{\mathrm{x}} = -\cos(\theta)\cos(90-\beta)\frac{1}{(dk_{\mathrm{n}}/d\sigma_{\mathrm{n}})}\ln\left(\frac{\sigma'_{\mathrm{n}}}{\sigma'_{\mathrm{ni}}}\right) \tag{12}$$

which can be written:

$$\Delta a_{\mathrm{x}} = -\cos(\theta)\cos(90-\beta)\frac{1}{(dk_{\mathrm{n}}/d\sigma_{\mathrm{n}})}\ln\left(1+\frac{\Delta\sigma'_{\mathrm{n}}}{\sigma'_{\mathrm{ni}}}\right) \tag{13}$$

and $\Delta\sigma_{\mathrm{n}}'$ and σ'_{ni} are given by Eqs. 7 and 8 respectively.

To evaluate Eq. 11 requires that values be specified for the stress ratio, k_0, and the stiffness characteristic, $dk_{\mathrm{n}}/d\sigma'_{\mathrm{n}}$. The stress ratio was allowed to range between 0.5 and 1.5. The values of the stiffness characteristic ranged between 25 and 75 mm^{-1}. These limits were chosen on the basis of the estimates compiled by Zangerl et al. (2008c) from laboratory or field tests on natural fractures subject to multiple loading cycles. The resulting upper and lower limits on the predicted annual change in length of baselines crossing Val Termine at the higher and lower elevations is shown for each single joint set in Fig. 12. The net deformation will be the combined response from all sets, although this may be less than the simple sum due to interaction.

The results indicate that values of stiffness characteristic lower than 25 mm^{-1} lead to predicted line-length changes that are larger than observed, even for high-stress situations. The value of 25 mm^{-1} is close to the lowest values derived from 3rd or later loading cycles in laboratory tests on natural fractures. Values as low as 3 mm^{-1} are reported by Zangerl et al. (2008c) for field tests on fractures at scales of tens of centimeters to tens of metres. Thus, the present analysis indicates that the observed deformations can be explained by assigning stiffness properties to the mapped fracture sets that are physically reasonable for the full range of stress states considered. There is no need to postulate that the fractures are highly compliant, as was suggested in earlier studies (El Tani and Bremen 2006). To extract more from the modeling would require a more detailed treatment of the problem, which includes the effects of topography on the stress, the effect of changes in fracture aperture on the total stresses, and fracture interaction. It is also uncertain as to whether the variation in water table is as large as assumed. It must be emphasised that the present model is only intended as a scoping calculation.

The mathematical model REROD (reversible rock-slope deformations)

A mathematical model of the reversible rock-slope deformations (REROD) has been developed which describes the relationship between the measured deformations across the valleys and nearby rainfall and snow height measurements. The model is based on transfer functions which describe the change in valley-crossing horizontal line-lengths resulting from aquifer depletion and recharge from snow melt and summer rainstorms. The geometry of the problem is the one that has already been shown in Fig. 8.

As described earlier, the relative displacement vector of the reflector at one end of a horizontal, valley-crossing line of length L with respect to the other is described by the components ΔL_{x}, ΔL_{y}, ΔL_{z} where x and y are horizontal and oriented valley-crossing and valley-parallel respectively, and z is vertical. Hereafter only changes in the length of the line, ΔL_x, will be of concern. A further subscript indicates the cause of the line-length change. Thus, ΔL_{xr} indicates rainfall-induced line-length change, ΔL_{xs} denotes snow melt induced changes, and ΔL_{xd} represents the line-length change caused by aquifer depletion (i.e. a fall in the groundwater level) between recharge episodes. Changes caused by a superposition of recharge processes are referred to as ΔL_{xrs}. A list of all parameters is given in Table 2.

The meteorological parameters of snow height and rainfall are not recorded at the same location and altitude as the deformations (see Fig. 1), and so they must be adjusted. Both climatic measurements are adjusted for altitude by using a linear relation for the dependence of precipitation on elevation in the Alps given by Beniston et al. (2003). The onset and progression of the groundwater recharge from snow melt depends on many factors such as snow-density and snow-water equivalent, ground temperature and freezing, altitude and exposition to solar radiation. Consequently the onset of groundwater recharge from snow melt at the modeled valley profiles may differ significantly from the onset of snow height reduction at the measurement station used for all profiles, which was station LUK-2. This difference is considered in the model by applying a local time constant (t_{d} in days) whose value is derived by performing a correlation analysis between the onset of the measured local deformation and the onset of observed snow height decrease at station LUK-2. Rainfall was measured at the crest of the dams near each of the four sites and was corrected to the altitude of the reflector pairs. Only rainfall that exceeded a daily threshold was considered to be an event. The threshold values used for each valley are listed in Table 3. The transfer functions that describe the line-length changes resulting from rainfall and snow melt at the four sites were constrained using data from a 3-year period, which is

 DOI 10.1007/s10040-011-0801-7

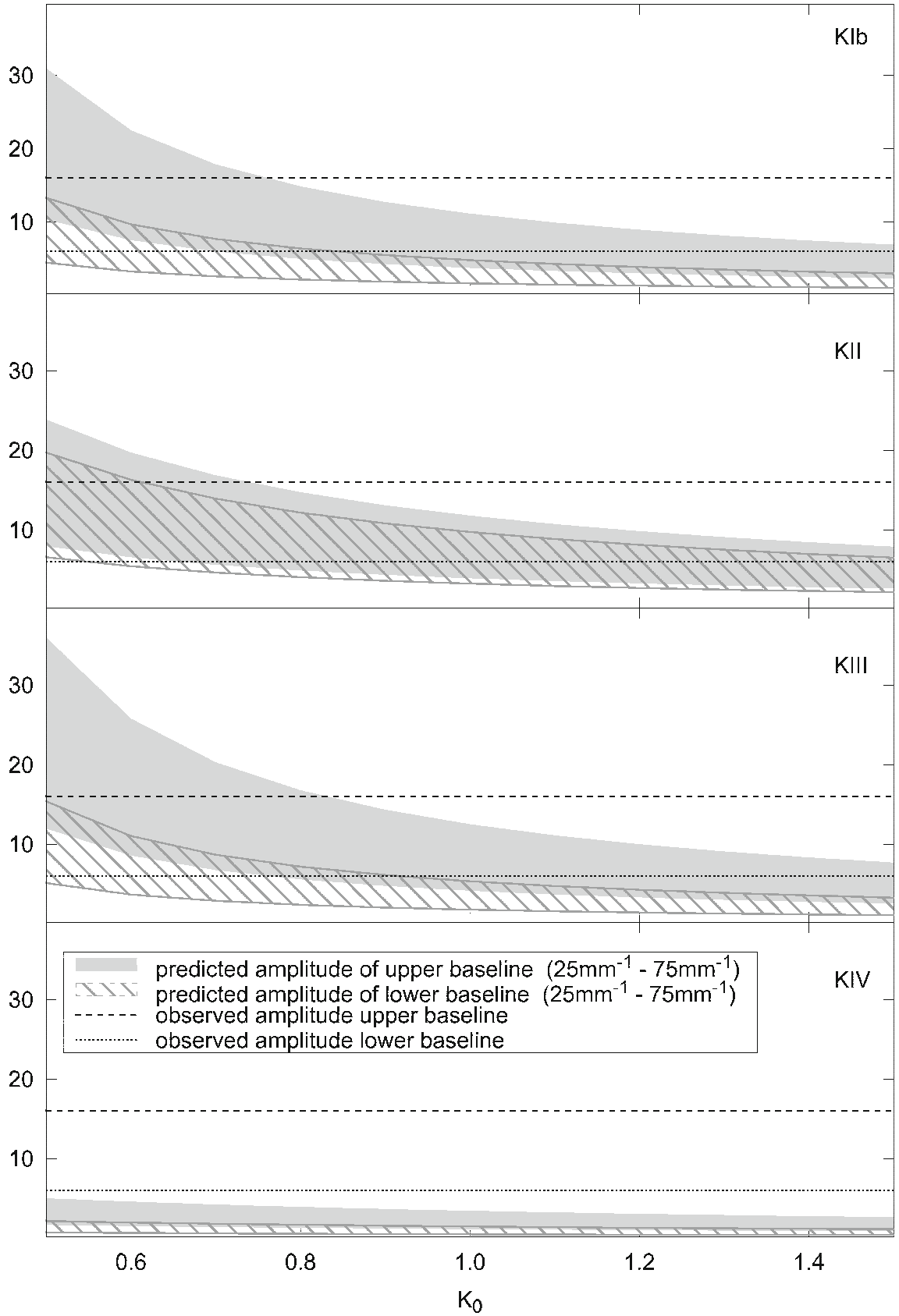

Fig. 12 Calculated amplitude of integrated deformation of the upper (L=542 m, *gray filled curve*) and lower (L=232 m, *hatched curve*) baselines for all four joint sets in Val Termine using Eqs. 13 and 14. The value for the stiffness characteristic is allowed to range from 25 to 75 mm^{-1}, which is a reasonable range of values, based on laboratory or field tests on natural fractures listed in Zangerl et al. (2008c)

 DOI 10.1007/s10040-011-0801-7

Table 2 Description of the model variables

Variable	Units	Description
L	$[L]$	Line-length of the modeled reflector pair
$\Delta L_{x,y,z}$	$[L]$	Relative displacement vector of one end of a valley-crossing baseline with respect to the other.
$\frac{\Delta L_{xr}(r)}{\Delta t}$	$[LT^{-1}]$	Time rate of change in line-length induced by rainfall
$\frac{\Delta L_{xs}(s_h)}{\Delta t}$	$[LT^{-1}]$	Time rate of change in line-length induced by snow melt
$\frac{\Delta L_{xd}}{\Delta t}$	$[LT^{-1}]$	Time rate of change in line-length induced by depletion of groundwater reservoir
$\frac{\Delta L_{xrs1}(r,s_h)}{\Delta t}$	$[LT^{-1}]$	Time rate of change in line-length induced by rainfall on snow layer in early winter
$\frac{\Delta L_{xrs2}(r,s_h)}{\Delta t}$	$[LT^{-1}]$	Time rate of change in line-length induced by rainfall during snow melt season
f_r	$[-]$	Factor for transformation of rainfall into line-length change
f_s	$[-]$	Factor for transformation of change in snow height into change in line-length
r_{min}	$[LT^{-1}]$	Minimum rainfall precipitation rate that the models account for
$S_{h\text{-}thin}$	$[L]$	Maximum snow height, through which rain could infiltrate
c_s	$[-]$	Fraction of snow that melts and infiltrates, when rain falls on it
c_{r1}	$[-]$	Fraction of rain that infiltrates through snow layer in early winter
c_{r2}	$[-]$	Fraction of rain that infiltrates through snow layer during snow melt phase
S_h	$[L]$	Measured snow height
r	$[LT^{-1}]$	Measured rainfall precipitation rate
a, b	$[L]$	Parameters that define the exponential depletion function
τ	$[T]$	Exponential time constant of the groundwater reservoir
t	$[T]$	Time in days (since model time step is in days)
$R\ (t)$	$[L^3T^{-1}]$	Rate of recharge
$Q\ (t)$	$[L^3T^{-1}]$	Rate of exfiltration
$S\ (t)$	$[L^3]$	Volume of water in reservoir
α	$[T^{-1}]$	Recession index
t_d	$[T]$	Local time shift of snow melt onset

described in section REROD model results and can be regarded as the model calibration period.

Precipitation, snow melt and groundwater reservoir depletion

Figure 13 shows the average rate of change of line length in Val Termine as a function of the rates of snow height change (Fig. 13a) and rainfall magnitude (Fig. 13b). For Fig. 13a, the rates of line-length change, $\Delta L_x/\Delta t$, were obtained by dividing the total line-length change during each snow melt season in late spring by the duration of the snow melt season. The corresponding estimates of the average rate of snow-height decrease were obtained by dividing the total height of snow melted per season by the duration of the snow melt phase. The data points plotted in Fig. 13a were derived from winters during the period 2004–2007, and are reasonably well-fitted by a linear relation. The slope of this relation will be denoted by f_s, and is positive (note that the abscissa, $\Delta s_h/\Delta t$, is plotted with more negative values to the right). For Fig. 13b, the line-length changes related to rainfall were obtained by taking daily averages of the length changes during rainstorm events, and plotting them against the corresponding average daily rainfall. The data points were derived from several rainstorm events that occurred in the years 2003 to 2006. These are also well-fitted by a linear relation, this time of slope f_r. Similar plots for the other sites are shown in the Appendix. All indicate that the relations between the rates of rainstorm precipitation or snow melt and the observed deformation rates can be taken as approximately linear. The corresponding slopes for all sites are listed in Table 3. Thus, for a given site, the values of the factors f_r and f_s relate the daily rainfall rate, r,

Table 3 Values of the model parameters that have been considered for the best-fit model

Variable	Units	Valley			
		Val Termine	Santa Maria	Nalps North	Nalps South
f_r	$[-]$	$-4.1 \cdot 10^{-2}$	$-7.1 \cdot 10^{-3}$	$-4.6 \cdot 10^{-3}$	$-8.9 \cdot 10^{-3}$
f_s	$[-]$	$4.1 \cdot 10^{-3}$	$1.4 \cdot 10^{-3}$	$1.1 \cdot 10^{-3}$	$2.4 \cdot 10^{-3}$
$abs(\frac{f_r}{f_s})$	$[-]$	10	5.1	4.2	3.7
r_{min}	[mm/d]	16.7	5	21.8	8
$h_{s\text{-}thin}$	[m]	0.7	1.1	1.3	1.2
c_s	$[-]$	0.0	0.1	0.3	0.05
c_{r1}	$[-]$	0.8	0.2	0.0	0.3
c_{r2}	$[-]$	0.9	0.2	0.0	0.3
a	$[m]$	0.018	0.0059	0.0051	0.006
b	$[m]$	−0.0078	−0.0012	−0.0025	−0.0023
$\tau = \frac{1}{\alpha}$	$[d]$	65	90	103	80
t_d	$[d]$	9	15	0	15
L	$[m]$	542	533	436	546

 DOI 10.1007/s10040-011-0801-7

and the snow-melt rate, $\Delta s_h/\Delta t$, respectively to the resulting line-length changes, ΔL_{xr} and ΔL_{xs}, through the equations:

$$\frac{\Delta L_{xr}(r)}{\Delta t} = f_r \cdot r \qquad \text{if } r > r_{min} \tag{14}$$

$$\frac{\Delta L_{xs}(s_h)}{\Delta t} = f_s \cdot \frac{\Delta s_h}{\Delta t} \qquad \text{if } \frac{\Delta s_h}{\Delta t} < 0 \tag{15}$$

where extension is taken as positive. Note that the models only account for rainfall that exceeds the minimum rainfall threshold r_{min} listed in Table 3. Since the rainfall recharge r in Eq. 14 is positive, and f_r is negative, then $\Delta L_{xy}/\Delta t$ is negative. In contrast, the snow-melt involves a negative change in snow height, $\Delta s_h/\Delta t$ in Eq. 15. Since f_s is positive, $\Delta L_{xs}/\Delta t$ is negative. Thus, both snow-melt and rainfall-related recharge produce contractional strains across the valleys.

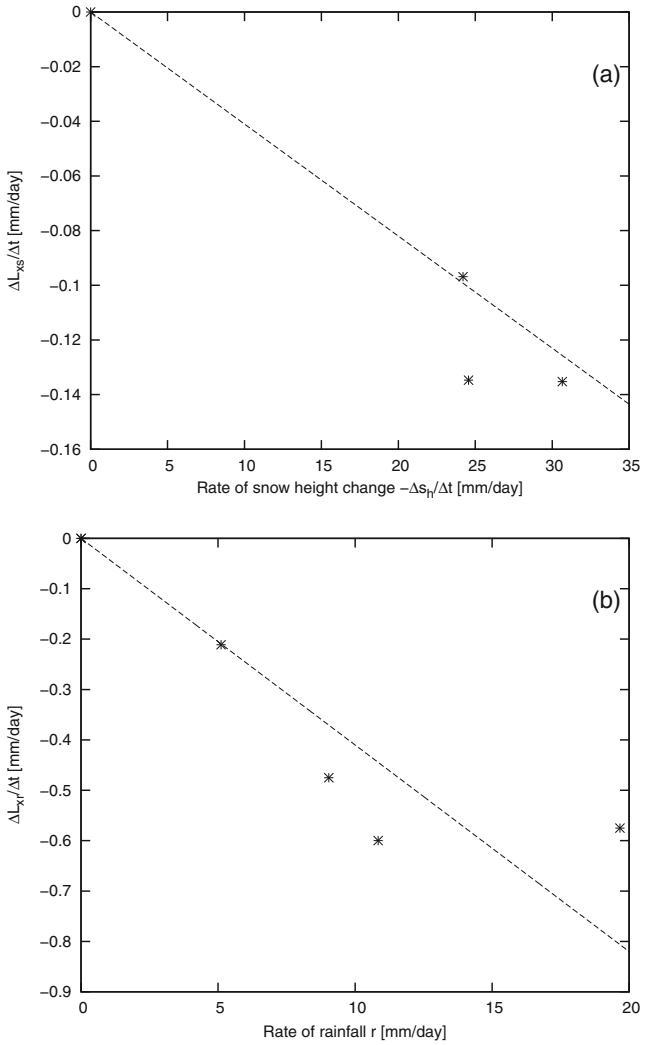

Fig. 13 **a** Relation between the daily change in baseline length (extension positive) and the corresponding daily change in snow height during snow melt averaged over the duration of snow-melt for each of the 3 years considered in the calibration period. The slope of the best-fitting linear trend, f_s, is positive. **b** Relation between daily change in baseline length and corresponding daily rainfall, both averaged over 7-day windows in which rainstorms occur during the 3-year calibration period. The data are reasonably well fit by a linear relation that has a negative slope, f_r. Note that both regression curves are forced to cross *(0,0)*, as the model should generate no snow-melt deformation or rainfall-induced deformation, when there is no snow melt or rainfall

Figure 14 shows the history of line-length change that occurs at times without any precipitation or snow melt for the example of Val Termine in winter 2004/2005. The curve has the form of an exponential given by:

$$\frac{\Delta L_{xd}}{\Delta t} = a \cdot (1 - e^{\frac{-t}{\tau}}) + b \tag{16}$$

where a and b are constants to be discussed later. In terms of the conceptual model, which holds that the deformations are due to a fluctuating water table, the exponential decay in line-length change can be understood as indicating that the reservoir depletion process has an exponential form. This implies that the rate of depletion of the reservoir always depends on the current state of the reservoir itself.

An exponential decay in depletion during periods of zero recharge follows readily from Boussinesq (1877). Maillet (1905) proposed that the discharge from an aquifer, $Q(t)$, varies linearly with the volume in storage, $S(t)$. That is,

$$Q(t) = \alpha \cdot S(t) \tag{17}$$

where α is a constant. During periods without recharge, conservation of mass implies that $Q(t) = -\delta S/\delta t$, and so for these periods Eq. 17 becomes,

$$\delta S/\delta t = -\alpha \cdot S(t) \tag{18}$$

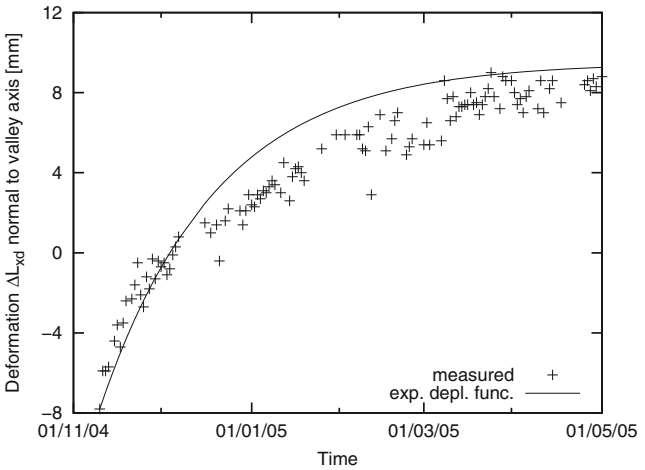

Fig. 14 Line-length changes measured across Val Termine during the winter of 2004/2005 when there was no recharge. The *crosses* denote measured changes and the *solid line* denotes the best-fitting exponential function computed from Eq. 16

DOI 10.1007/s10040-011-0801-7

This can be integrated to give

$$S(t) = S_0 \cdot e^{-\alpha \cdot t} \tag{19}$$

Where S_0 is the volume in storage at time t=0. Using Eq. 17, this may be written,

$$Q(t) = Q_0 \cdot e^{-\alpha \cdot t} \tag{20}$$

Where Q_0 is the discharge from the reservoir at t=0. The constant α is called the recession index, and is often expressed by the recession constant $k=e^{-\alpha}$. The validity of Eq. 16 and hence the exponential form of the discharge equation for the depletion of groundwater in valley flanks was demonstrated by Payton Gardner et al. (2010) for the case when the head change is small compared to aquifer thickness so that the flow is predominantly one-dimensional (i.e. lateral). In this case, the Boussinesq equation describing flow can be linearized to give (Manga 1997)

$$\frac{\delta h}{\delta x} = \frac{K_x h_0}{S_y} \frac{\delta^2 h_1}{\delta^2 x^2} + \frac{N(x,t)}{S_y} \tag{21}$$

where $K_x h_0/S_y$ is hydraulic diffusivity, $N(x,t)$ represents the recharge of the reservoir, $h_1=h(x) - h_0$ and S_y is the specific yield. Assuming an aquifer that is initially fully saturated with a fully penetrating stream with constant head s_h at x=0 and $h=h_0$ at $x=L$, Boussinesq (1877) derived an analytical solution of Eq. 21, using the Fourier's method, that for large times yields:

$$q = 2K_x h_0 (h_0 - h_s) L^{-1} e^{-\pi^2 K_x h_0 t/4 S_y L^2} \tag{22}$$

This has the same form as the exponential Eq. 16, and shows that the recession index α is proportional to hydraulic diffusivity. Thus, the exponential nature of the line-length changes during periods without recharge described by Eq. 16 almost certainly reflects groundwater depletion (lowering of the water table) within the flanks of the valley.

During depletion, the line-lengths extend and the valley flanks move apart. The maximum extension occurs when discharge rate $Q(t)$ and storage $S(t)$ reach their minimum. The parameter a in Eq. 16 physically represents the largest possible change in groundwater level elevation. The parameter b sets the minimum value of the exponential function and thus represents the highest possible elevation of the recharged groundwater level. The parameter τ can be regarded as the depletion time constant of the groundwater reservoir and equals $1/\alpha$. Averaged values for a, b and τ from exponential functions that were fitted to the measured deformations during the depletion phases of the 3-year calibration period are derived for every valley section and are listed in Table 2.

Superposition of recharge processes

Significant rainstorms sometimes occur in early winter, after a first thin snow cover has developed. Under certain conditions, the thin snow cover can melt and infiltrate together with the rain into the subsurface. Similarly, rainstorm events that occur during the snow melt phase can increase the amount of recharge that reaches the water table. Initial modeling of the displacements demonstrated the need to include superposition of rainstorm and snow melt events, which was implemented in the code using Eqs. 23 and 24. Specifically, in the case where rainstorms in early winter fall on and partially melt a thin snow layer of thickness less than $s_{h\text{-}thin}$, the line-length change resulting from the combined recharge is computed from:

$$\frac{\Delta L_{xrs1}(r,h_s)}{\Delta t} = (c_{r1} \cdot f_r \cdot r) + \left(c_s \cdot f_s \cdot \frac{s_h}{\Delta t}\right) \text{if } s_h < s_{h-thin} \tag{23}$$

whereas in the case where rainstorms occur during the snow melt period, the deformational response is computed from:

$$\frac{\Delta L_{xrs2}(r,h_s)}{\Delta t} = (c_{r2} \cdot f_r \cdot r) + \left(f_s \cdot \frac{\Delta s_h}{\Delta t}\right) \quad \text{if } s_h < s_{h-thin} \tag{24}$$

Equations 23 and 24 are applied if the snow layer is thinner than $s_{h\text{-}thin}$. In this case, rainfall is assumed to be able to percolate through and melt a part of the thin snow layer. The factor c_{r1} in Eq. 23 represents the fraction of rainfall that infiltrates into the ground, the remainder running-off directly and c_s is the fraction of the snow that melts and infiltrates with the precipitated water. In case of rainstorms occurring during the snow-melt phase (Eq. 24), a prescribed fraction of rainfall c_{r2} is allowed to infiltrate. This is in addition to the amount of water that infiltrates as a consequence of the snow melt phase.

The values for each of the variables $s_{h\text{-}thin}$, c_s, c_{r1} and c_{r2} were allowed to range over reasonable bounds for every valley section. The set of values used in the final model for each valley section was found by a simple brute force search method in which the correlation between predicted and observed deformations was computed for all possible combinations of the four parameters within their assigned ranges. The set of values that yielded the best correlation of modeled and observed surface deformations as measured by the highest Pearson's coefficient was adopted as the best-fit model.

REROD algorithm

A simplified flowchart of the algorithm implemented in the code is shown in Fig. 15. The rectangular boxes denote model actions and the oval boxes represent yes/no-queries. Branches to the left stand for the actions that follow positive answers to the queries, branches to the right are the actions that are taken in case of negative answers.

In a first step, the input data sets of snow height and rainfall measurements are read in and interpolated to the elevation of the model area. Then a loop with a step size

 DOI 10.1007/s10040-011-0801-7

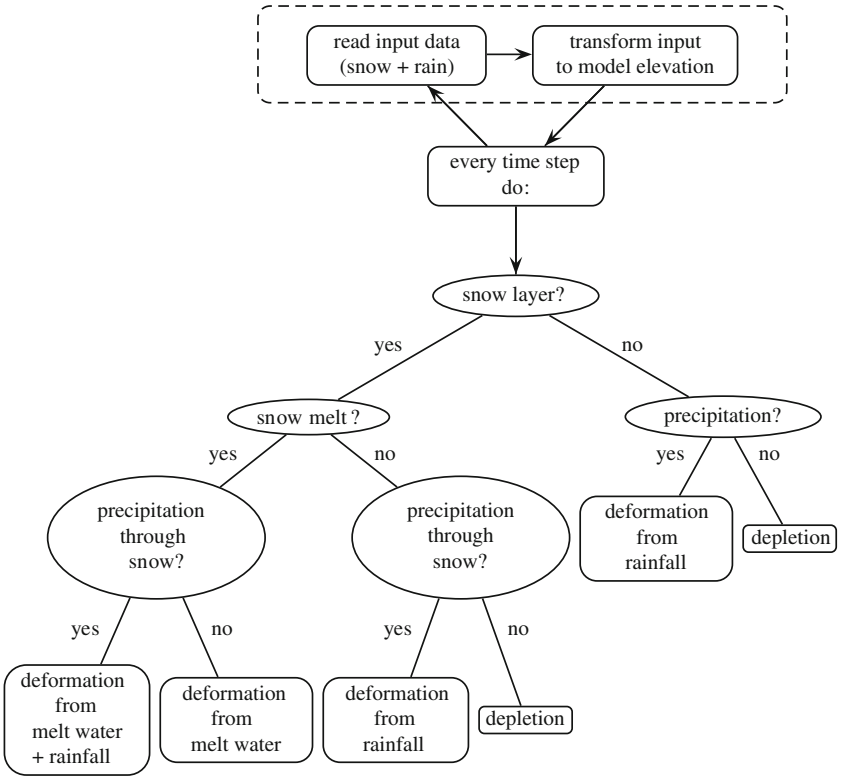

Fig. 15 Simplified flowchart of the model algorithm. *Rectangular boxes* denote model actions, and *oval boxes* represent yes/no queries. Branches continue *to the left* for positive answers, and *to the right* for negative answers

of 1 day is run over the input data. During every time step the model checks whether a snow layer exists in the model area. If no snow is present, then deformation comes from either the depletion of the groundwater reservoir (Eq. 16), or from recharge by rainstorms (Eq. 14). In case of reservoir depletion the model first computes the time t of Eq. 16, which represents the time lag from the last recharge event and uses this value in Eq. 16 to calculate the deformation induced by depletion. If, however, a snow layer exists, then deformation can be generated in several ways, including superposition of different processes. A first check establishes whether the existing snow layer is in the melting phase. If the snow layer is not in the melting phase, the next check is done to find out whether snow height is less than the $s_{\text{h-thin}}$ limit that would allow rainfall to infiltrate through the snow layer. Depending on the result of this check, deformation can be generated either by depletion of the groundwater reservoir only (Eq. 16), or by rainfall that infiltrates through a thin snow layer and melts parts of this thin snow layer (Eq. 23). If the existing snow layer is in the melting phase, then the model algorithm checks again whether the snow height exceeds the limiting height for rainfall percolation. If yes, then deformation is generated by the infiltration of snow-melt water only (Eq. 15). However, if the height of the snow layer is below the prescribed threshold for percolation, then the rainfall adds to the infiltration from snow melt (Eq. 24). A grid search routine in which the free variables were allowed to vary within defined ranges was used to find the model that yields the best correlation between the modeled and observed line-length changes.

REROD model results

The combinations of parameters that were found to yield the best results for each site are listed in Table 3. Modeled and observed line-length changes for the four studied profiles are shown in Fig. 16. The green line denotes the measured line-length changes normal to the valley axis for the reflector pairs. The best-fitting predictions for models with and without superposition of different recharge processes are shown in solid red and dashed blue respectively. The dashed black and brown lines represent the distance to the advancing tunnel face of the east and west tunnel tubes. The arrows indicate the 3-year model calibration periods for each studied profile. It is evident that a significant improvement in fit is obtained by including superposition. The quality of fits is very good, even outside the 3-year time window used to calibrate the model. The best results were achieved for Val Termine and Santa Maria where daily displacement measurements were available for model calibration. The differences between predicted and measured displacements at these sites are of the order of 1–2 mm. For the other two profiles, at Nalps-North and Nalps-South, where line-length changes were available only every 2 weeks, the discrepancies between measured and predicted series tend to be slightly larger (2–3 mm). These larger differences are all the more

 DOI 10.1007/s10040-011-0801-7

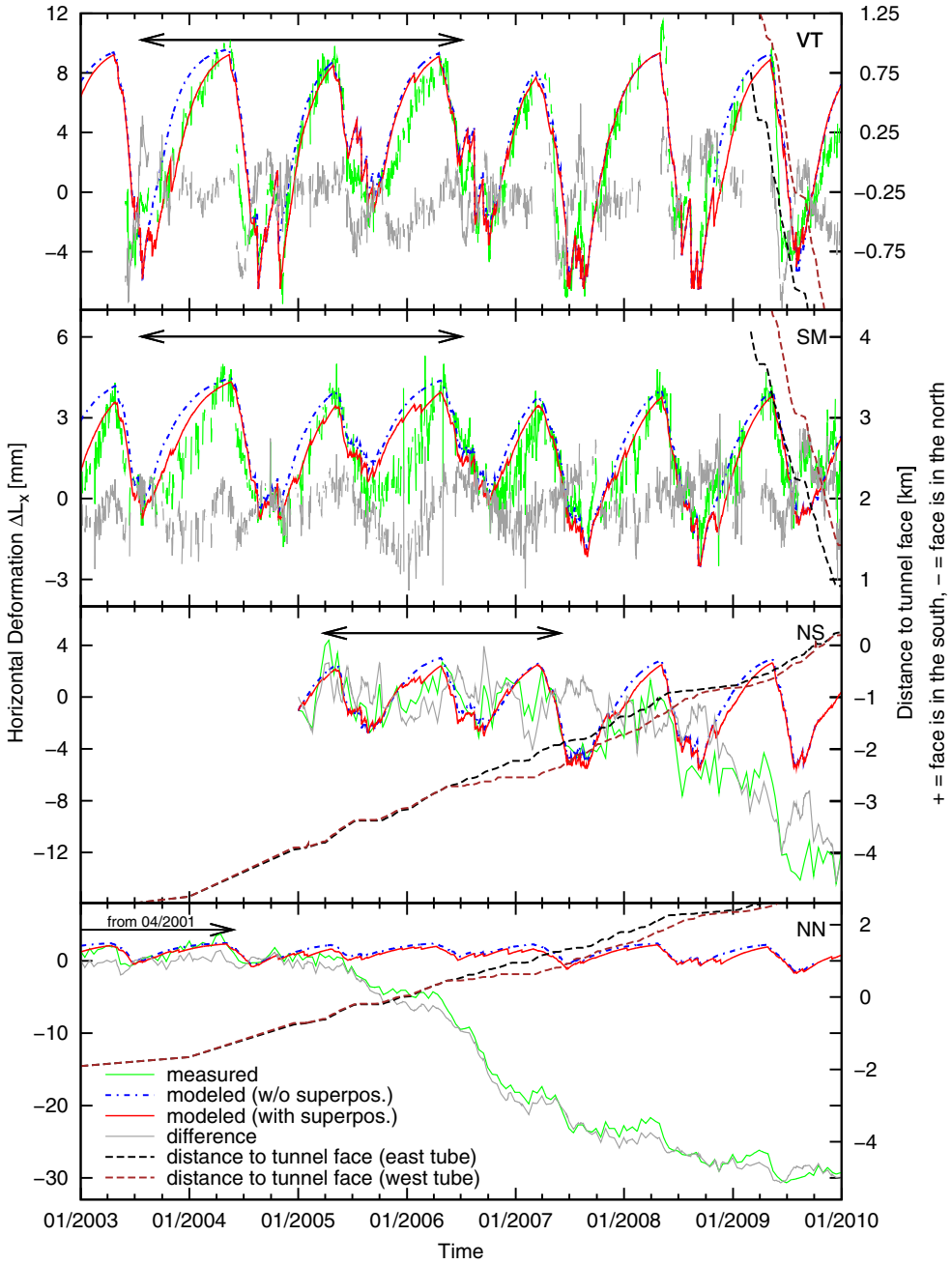

Fig. 16 Comparison of observed and model-predicted line-length changes between reflector pairs crossing the valleys at Val Termine (*VT*), Santa Maria (*SM*), Nalps South (*NS*) and Nalps North (*NN*). The *green line* denotes observed, unsmoothed changes. The *dashed blue lines* are changes predicted by the best-fitting model without superposition of recharge processes, whilst the *solid red lines* are for the best-fitting models with superposition. The 3-year period used for calibrating the models is indicated in each plot with *black arrows*. The *gray line* shows the measured line-length change with the predicted change from the best-fitting model removed and shows the signal due to tunneling for NS and NN. The *black dashed line* shows the distance of the tunnel face at the east tube to the monitoring profiles, whilst the *brown dashed line* shows the distance of the tunnel face at the west tube to the monitoring profiles

significant because the amplitudes of the natural deformation signals at these sites are smaller.

The residual series obtained by subtracting the predicted line-length change series derived from the model with superposition from the measured series are shown by the gray lines in Fig. 16. The removal of the natural deformation signal improves the resolution of the line-length changes arising from tunneling activity, which can be seen to develop beginning in mid-2005 for Nalps-North and early-2008 for Nalps-South. The black dashed line in Fig. 16 shows the distance of the tunnel face to the monitoring profiles.

Discussion and conclusions

The physical and mathematical modeling results demonstrate that the reversible deformations observed within the

 DOI 10.1007/s10040-011-0801-7

Table 4 The lithology of the study area, from Schneider (1993) and field mapping

Valley	Predominant rock types	Description
Val Termine	Striped gneisses ("Streifengneise")	Quartz-feldspar rich ortho-gneisses
Santa Maria	Medelser granites	Granites with significant degree of jointing
Val Nalps	"Paradise gneisses"	Gneisses with heterogenous internal composition

alpine valleys in the study area are due to natural fluctuations in groundwater level within the valley flanks, as proposed by El Tani and Bremen (2006) and Loew et al. (2007). In Val Termine the spring-line measurements indicate that the water table falls to almost the level of the valley. While recharge happens relatively fast, within 2–

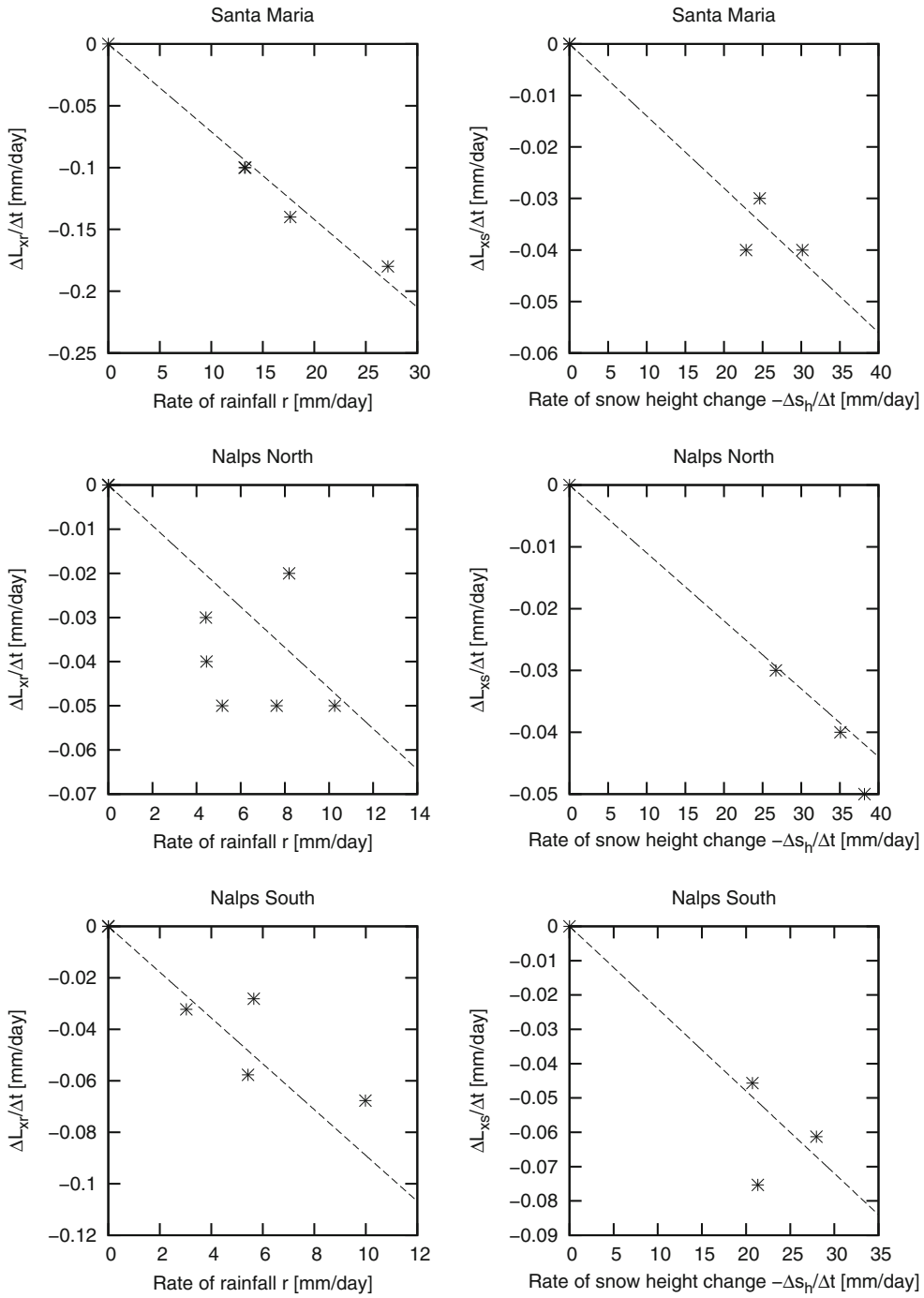

Fig. 17 Deformation as a function of snow melt rate (*left panel*) or rain fall rate (*right panel*) for the cross sections at Santa Maria, Nalps North and Nalps South. *Dashed line* shows the linear relation for each case, that has been applied in the mathematical model, as found by the brute-force optimization

 DOI 10.1007/s10040-011-0801-7

3 months after the onset of snow melt or during prolonged rainstorms, reservoir depletion essentially acts during the remaining time of the year.

Other coupled mechanisms such as annual thermal forcing almost certainly produce ground-surface deformation as well. However, as discussed in El Tani and Bremen (2006 and Rossinelli (2007) no clear correlation between air temperature and the change in valley-crossing line lengths is evident. Braeker (2006) implies that possible thermal induced deformations would be in the order of several tenths of a millimeter. Numerical modelling studies of the displacements induced by annual variations in surface temperature on alpine topography by Gischig et al (2011) indicate horizontal relative displacements of the valley flanks of the order of a few millimeters. Collectively, these results suggest that the thermally induced valley-crossing horizontal displacements at annual periods are an order of magnitude smaller than the observed variations.

The response time of the deformation signal to the recharge events was studied and shown to be less than 1 day. This demonstrates that water infiltration through the unsaturated fractured bedrock of Val Termine occurs very fast. As shown in Masset and Loew (2010), steep alpine valleys in crystalline bedrock show significant unloading and physical weathering phenomena which lead to interconnected open fractures with very high effective hydraulic conductivity in the uppermost 200–400 m.

Simple analytical calculations, which do not account for the interaction of different joint sets or coupled poro-elastic effects, suggest that the measured deformations in Val Termine are largely generated by changes in the aperture of fractures in response to pore-pressure variations from groundwater recharge and drainage. It is likely that the steeply dipping joint set KIII, which strikes sub-parallel to the valleys, contributes the most to the observed horizontal deformations, whereas the other joint sets are more important for the vertical deformation component.

The amplitude of the observed natural displacements and strains varies from valley to valley (Fig. 9). The causes underpinning the variations are not yet understood. Possible factors are:

- Different joint characteristics of the valleys (especially spacing, stiffness, dip angle and orientation with respect to the plane in which the reflectors of the monitoring network lie)
- The geometry of the valley slopes, such as steepness and scale of relief, and the exposition of the terrain
- Differences in hydromechanical rock mass properties, especially hydraulic conductivity and stiffness
- Differences in soil cover and recharge
- Differences in climatic conditions, especially altitude dependent precipitation and snow melt

All four valley-crossing profiles in Fig. 2 have a similar slope for the flanks but differ in terms of their relief (i.e. the elevation differences between the valley floors and the ridges). The relief is lowest at Val Termine, which also shows the largest amplitudes of horizontal and vertical deformations normal to the valley axis. Higher relief will tend to result in higher effective stresses acting on the fractures within the flanks at the level of the valley, and these would be stiffer as a consequence. On the other hand, higher relief could promote larger variations in groundwater level leading to larger variations in pore pressure within the flanks at the level of the valley floor. Within the physical model, the two effects precisely balance each other so that the aperture change of fractures was independent of overburden. Whether the groundwater level attains the maximum possible variation during the annual cycle (i.e. from the surface to the valley floor) will depend on other factors such as the hydraulic conductivity distribution and storage of the rock mass.

The possible correlation between geology (see Table 4) and the signal amplitudes is the subject of on-going studies. The valleys at the four sites considered lie at different elevations of between 1,600 and 2,050 m a.s.l. (Fig. 2). Thus, it is likely there will be significant differences in precipitation, both as rain and snow (Uttinger 1951; Beniston et al. 2003).

The mathematical model was developed as a tool for removing the unexpectedly large annual component of the measured deformation signal and so improves the detectability of deformations associated with tunneling activity. The approach has been very successful, as can be seen by the residual series for the four sites. Residuals lie in the order of 1–3 mm, which might partly be due to the noise level that is induced by the measurement devices and partly reflects uncertainties of the model assumptions.

Acknowledgements The authors would like to thank H. Ehrbar, A. Ryf and F. Ebneter of AlpTransit for the long-term support of this project. We also appreciate important contributions from NOK (M. Lutz), Swissphoto (M. Studer), SLF (N. Dawes) and WSL (M. Zappa). The authors would further like to thank the anonymous reviewers for providing constructive comments and suggestions.

Appendix

Here is shown the linear relationships between deformation and snow melt rate or rainfall precipitation rate for Santa Maria, Nalps North and Nalps South. In the case of Santa Maria, data for calibration is taken from the years 2003–2006, for Nalps North, from the years 2001–2004 and for Nalps South from the years 2005–2007. The dashed lines show the linear relation that was used in the models as found by the grid search optimization. Deviations of the linear relation used for the models and the linear relation implied by the data points might arise from errors induced by transformation of snow height or rainfall data from the elevation they were recorded to the elevation of the modeled sensor pairs. Furthermore, for the profiles Nalps North and Nalps South, deformation data only have a 14-day resolution, which limits the accuracy of the data points in the plots (Fig.17).

References

AlpTransit Gotthard AG (2003) Überwachung KVR-Stauanlagen. Jahresbericht per 31.12.2002, ARGE Los 349 [Monitoring at the KVR reservoir sites. Annual report from 31.12.2002]., ARGE Los 349, AlpTransit Gotthard

Beniston M, Keller F, Goyette S (2003) Snow pack in the Swiss Alps under changing climatic conditions: an empirical approach for climate impacts studies. Theor Appl Climatol 74(1):19–31

Boussinesq J (1877) Essai sur la théorie des eaux courantes, du mouvement nonpermanent des eaux souterraines [Essay on the theory of flowing waters and the transient movement of groundwater]. Acad Sci Inst Fr 23:252–260

Braeker F (2006) Anspruchsvolle Ueberwachungsaufgabe beim Projekt AlpTransit Gotthard [Challenging monitoring campaigns in the framework of the AlpTransit Gotthard project]. Geomatik Schweiz 6:314–320

El Tani M, Bremen R (2006) Val Termine cyclic deformation due to seasonal variation of water table. Golden Rocks 2006, The 41st US Symposium on Rock Mechanics (USRMS), 17–21 June 2006, Golden, CO

Evans K, Kohl T, Rybach L, Hopkirk R (1992) The effects of fracture normal compliance on the long term circulation behaviour of a hot dry rock reservoir: a parameter study using the new fully-coupled code fracture. Geotherm Resour Counc Trans 16:449–456

Gischig V, Moore JR, Evans E, Amann F, Loew S (2011) Thermomechanical forcing of deep rock slope deformation, part I: conceptual study of a simplified slope. J Geophy Res Earth Surf. doi:10.1029/2011JF002006

Gubler E (2003) Beschreibung zum Programm LTOP Version 94 [Description of the LTOP software version 1994]. Bundesamt für Landestopographie, Berne, Switzerland

Loew S, Ebneter F, Bremen R, Herfort M, Luetzenkirchen V, Matousek F (2007) Annual opening and closure of alpine valleys,Felsbau. Rock Soil Eng 25(5):60–65

Lombardi G (1992a) The FES rock mass model, part 1. Dam Eng 3:49–76

Lombardi G (1992b) The FES rock mass model, part 2: some examples. Dam Eng 3:201–221

Lombardi G (2004) Ground-water induced settlements in rock masses and consequences for dams. In: IALAD-Integrity Assessment of Large Concrete Dams Conference, Zurich, 24 September 2004

Maillet E (1905) Essais d'hydraulique souterraine et fluviale [On the hydrology of groundwater and rivers]. Librairie Sci., Hermann, Paris, 218 pp

Manga M (1997) A model for discharge in spring-dominated streams and implications for the transmissivity and recharge of quaternary volcanics in the Oregon cascades. Water Resour Res 33(8):1813–1822

Masset O, Loew S (2010) Hydraulic conductivity distribution in crystalline rocks, derived from inflows to tunnels and galleries in the Central Alps, Switzerland. Hydrogeol J 18(4):863–891

Payton Gardner W, Susong DD, Kip Solomon D, Heasler H (2010) Snowmelt hydrograph interpretation: revealing watershed scale hydrologic characteristics of the Yellowstone Volcanic Plateau. J Hydrol 383(3–4):209–222

Rossinelli S (2007) Zeitreihenanalyse der geodätischen Staumauerüberwachung [Time series analysis of geodetic data from monitoring of storage lake dam walls]. Diploma Thesis, Institute for Geodaesy and Photogrammetry, ETH Zurich, Switzerland

Schneider T (1993) Auswertung der Detailkartierungen 1991/2 (AlpTransit) [Analysis of detailed mapping campaigns 1991/2 (AlpTransit)]. Tech Rep, Schneider,Stans, Switzerland

Studer M, Braeker F (2007) Kombinierter Einsatz von automatischen und manuellen Messmethoden bei einem Langzeitmonitoring [Combined application of automated and manual monitoring methods used in long-term monitoring]. In: 15th International Course on Engineering Surveying, Graz, Austria, April 2007

Uttinger H (1951) Zur Hoehenabhaengigkeit der Niederschlagsmenge in den Alpen [On the elevation dependence of precipitation volume in the Alps]. Theor Appl Climatol 2(4):360–382

Zangerl C, Eberhardt E, Loew S (2003) Ground settlements above tunnels in fractured crystalline rock: numerical analysis of coupled hydromechanical mechanisms. Hydrogeol J 11:162–173

Zangerl C, Evans K, Eberhardt E, Loew S (2008a) Consolidation settlements above deep tunnels in fractured crystalline rock: part 1, investigations above the Gotthard highway tunnel. Int J Rock Mech Min Sci 45(8):1195–1210

Zangerl C, Eberhardt E, Evans K, Loew S (2008b) Consolidation settlements above deep tunnels in fractured crystalline rock: part 2, numerical analysis of the Gotthard highway tunnel case study. Int J Rock Mech Min Sci 45(8):1211–1225

Zangerl C, Evans K, Eberhardt E, Loew S (2008c) Normal stiffness of fractures in granitic rock: a compilation of laboratory and in-situ experiments. Int J Rock Mech Min Sci 45(8):1500–1507